

Wasserstein Distances for Stereo Disparity Estimation

Divyansh Garg¹ Yan Wang¹ Bharath Hariharan¹
 Mark Campbell¹ Kilian Q. Weinberger¹ Wei-Lun Chao²
¹Cornell University, Ithaca, NY ²The Ohio State University, Columbus, OH
 {dg595, yw763, bh497, mc288, kqw4}@cornell.edu chao.209@osu.edu

Abstract

Existing approaches to depth or disparity estimation output a distribution over a set of pre-defined discrete values. This leads to inaccurate results when the true depth or disparity does not match any of these values. The fact that this distribution is usually learned indirectly through a regression loss causes further problems in ambiguous regions around object boundaries. We address these issues using a new neural network architecture that is capable of outputting arbitrary depth values, and a new loss function that is derived from the Wasserstein distance between the true and the predicted distributions. We validate our approach on a variety of tasks, including stereo disparity and depth estimation, and the downstream 3D object detection. Our approach drastically reduces the error in ambiguous regions, especially around object boundaries that greatly affect the localization of objects in 3D, achieving the state-of-the-art in 3D object detection for autonomous driving. Our code will be available at <https://github.com/Div99/W-Stereo-Disp>.

1 Introduction

Depth estimation from stereo images is a long-standing task in computer vision [30, 36]. It is a key component of many downstream problems, ranging from 3D object detection in autonomous vehicles [8, 21, 33, 42, 54] to graphics applications such as novel view generation [23, 55]. The importance of this task in practical applications has led to a flurry of recent research. Convolutional networks have now superseded more classical techniques and led to significant improvements in accuracy [4, 27, 43, 57].

These techniques estimate depth by finding accurate pixel correspondences and estimating the *disparity* between their X -coordinates, which is inversely proportional to depth. Because pixels have integral coordinates, so does the estimated disparity — causing even the resulting depth estimates to be discrete. This introduces inaccuracy, as the ground truth disparity and depth are naturally real-valued. This discrepancy is typically addressed by predicting a *categorical distribution* over a fixed set of discrete values, and then computing the *expected* depth from this distribution, which can in theory be any arbitrary real value (within the range of the set) [4, 14, 43, 54, 57].

In this paper, we argue that such a design choice may lead to inaccurate depth estimates, especially around object boundaries. For example, in Figure 1 we show the pixels (back-projected into 3D

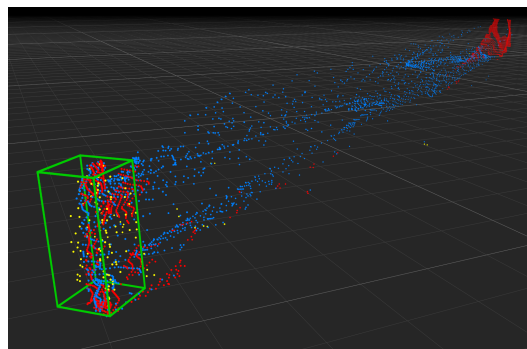


Figure 1: **The effect of our continuous disparity network (CDN).** We show a person (green box) in front of a wall. The blue 3D points are obtained using PSMNet [4]. The red points from our CDN model are much better aligned with the shape of the objects: they do not suffer the streaking artifacts near edges. Yellow points are from the ground truth LiDAR. (One floor square is $1\text{m} \times 1\text{m}$.)

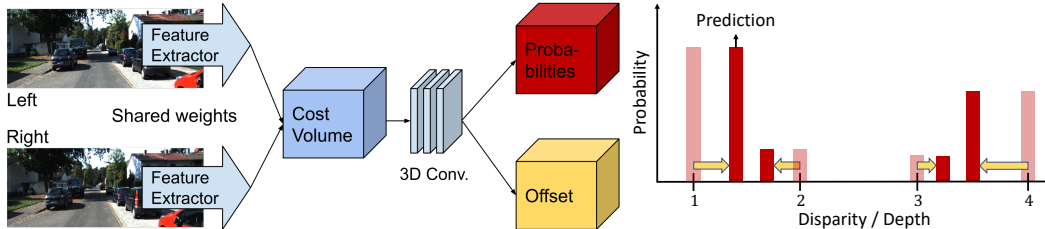


Figure 2: **Continuous disparity network (CDN)**. We propose to predict a *real-value* offset (yellow arrows) for each pre-defined discrete disparity value (e.g., $\{1, 2, 3, 4\}$), turning a categorical distribution (magenta bars) to a continuous distribution (red bars), from which we can output the mode disparity for accurate estimation.

using the depth estimates) along the boundary between a person in the foreground at 30m depth and a wall in the background at 70m depth. The predicted depth distribution of these border pixels is likely to be multi-modal, having two peaks around 30 and 70 meters. Simply taking the mean outputs a low probability value in between the two modes (e.g., 50m). Such “smoothed” depth estimates can have a strong negative impact on subsequent 3D object detection, as they “smear” the pedestrian around the edges towards the background (note the many blue points between the wall and the pedestrian). A bounding box including all these trailing points, far from the actual person, would strongly misrepresent the scene’s geometry. What may further aggravate the problem is how the distribution is usually learned. Existing approaches mostly learn the distribution via a regression loss: minimizing the distance between the mean value and the ground truth [14, 54]. In other words, there is no direct supervision to teach the model to assign higher probabilities around the truth depth.

To address these issues, we propose a novel neural network architecture for stereo disparity estimation that is capable of outputting a distribution over *arbitrary* disparity values, from which we can directly take the mode and bypass the mean. As with existing work, our model predicts a probability for each disparity value in a pre-defined, discrete set. Additionally, it predicts a real-valued *offset* for each discrete value. This is a simple architectural modification, but it has a profound impact. With these offsets, the output is converted from a discrete categorical distribution to a *continuous* distribution over disparity values: a mixture of Dirac delta functions, centered at the pre-defined discrete values shifted by predicted offsets¹. This simple addition of predicted offsets allows us to use the mode as the prediction during inference, instead of the mean, guaranteeing that the predicted depth has a high estimated probability. Figure 2 illustrates our model, **continuous disparity network (CDN)**.

Next, we propose a novel loss function that provides a more informative objective during training. Concretely, we allow uni- or multi-modal ground truth depth distributions (obtained from nearby pixels) and represent them as (mixtures of) Dirac delta functions. The learning objective is then to minimize the divergence between the predicted and the ground truth distributions. Noting that the two distributions might not have a common support, we apply the Wasserstein distance [41] to measure the divergence. While computing the exact Wasserstein distance of arbitrary distributions can be time-consuming, computing it for one-dimensional distributions (e.g., distributions of one-dimensional disparity) enjoys efficient solutions, creating negligible training overhead.

Our proposed approach is both mathematically well-founded and practically extremely simple. It is compatible with most existing stereo depth or disparity estimation approaches — we only need to add an additional offset branch and replace the commonly used regression loss by the Wasserstein distance. We validate our approach using multiple existing stereo networks [4, 54, 57] on three tasks: stereo disparity estimation [27], stereo depth estimation [9], and 3D object detection [9]. The last is a downstream task using stereo depth as the input to detect objects in 3D. We conduct comprehensive experiments and show that our algorithm leads to significant improvement in all three tasks.

2 Background

Stereo techniques rely on two cameras oriented parallel and translated horizontally relative to each other [49, 56]. In this setting, for a pixel (u, v) in one image, the corresponding pixel in the second

¹Our work is reminiscent of G-RMI pose estimator [30], which predicts the heatmaps (at fixed locations) and offsets for each keypoint. Our work is also related to one-stage object detectors [22, 24, 35] that predict the class probabilities and box offsets for each anchor box.

image is constrained to be at $(u + D(u, v), v)$, where $D(u, v)$ is called the *disparity* of the pixel. The disparity is inversely proportional to the *depth* $Z(u, v)$: $D(u, v) = \frac{f \times b}{Z(u, v)}$, where b is the translation between the cameras (called the *baseline*) and f is the focal length of the cameras. Stereo depth estimation techniques typically first estimate disparity in units of pixels and then exploit the reciprocal relationship to approximate depth. The basic approach is to compare pixels (u, v) in the left image I_l with pixels $(u, v + d)$ in the right image I_r for different values of d , and find the best match. Since pixel coordinates are constrained to be integers, d is constrained to be an integer as well. The estimated disparity is thus an integer, forcing the estimated depth to be one of a few discrete values.

Instead of producing a single integer-valued disparity value, modern pipelines produce a *distribution* over these possible disparities [4, 14]. They do this by constructing a 4D *disparity feature volume*, C_{disp} , in which $C_{\text{disp}}(u, v, d, :)$ is a feature vector that captures the difference in appearance between $I_l(u, v)$ and $I_r(u, v + d)$. This feature vector can be, for instance, the concatenation of the feature vectors of the two pixels, in turn obtained by running a convolutional network on each image. The disparity feature volume is then passed through a series of 3D convolutional layers, culminating in a cost for each disparity value d for each pixel, $S_{\text{disp}}(u, v, d)$ [4]. By taking softmax along the disparity dimension, one can turn $S_{\text{disp}}(u, v, d)$ into a probability distribution [26]. Because we only consider integral disparity values, this distribution is a categorical distribution over the possible disparity values (e.g., $d \in \{0, \dots, 191\}$). One can then obtain the disparity $D(u, v)$, for example, by $\text{argmax}_d \text{softmax}(-S_{\text{disp}}(u, v, d))$. However, in order to obtain continuous disparity estimates beyond integer-valued disparities, [4, 14, 43, 57] apply the following weighted combination (i.e., mean),

$$D(u, v) = \sum_d \text{softmax}(-S_{\text{disp}}(u, v, d)) \times d. \quad (1)$$

The whole neural network can be learned end-to-end, including the image feature extractor and 3D convolution kernels, to minimize the disparity error (on one image)

$$\sum_{(u,v) \in \mathcal{A}} \ell(D(u, v) - D^*(u, v)), \quad (2)$$

where ℓ is the smooth L1 loss, D^* is the ground truth map, and \mathcal{A} contains pixels with ground truths.

Recently, [54] argue that learning with Equation 2 may over-emphasize nearby depths, and accordingly propose to learn the network directly to minimize the depth loss. Specifically, they constructed depth cost volume $S_{\text{depth}}(u, v, z)$, rather than $S_{\text{disp}}(u, v, d)$, and predicted the continuous depth by

$$Z(u, v) = \sum_z \text{softmax}(-S_{\text{depth}}(u, v, z)) \times z. \quad (3)$$

The entire network is learned to minimize the distance to the ground truth depth map Z

$$\sum_{(u,v) \in \mathcal{A}} \ell(Z(u, v) - Z^*(u, v)). \quad (4)$$

In this paper, we argue that the design choices to output continuous values (Equation 1 and Equation 3) can be harmful to pixels in ambiguous regions, and the objective functions for learning the networks (Equation 2 and Equation 4) do not directly match the predicted distribution to the true one. The most similar work to ours is [58], which learns the network with a distribution matching loss on $\text{softmax}(-S_{\text{disp}}(u, v, d))$; however, they still need to apply Equation 1 to obtain continuous estimates. Luo et al. [26] also learned the network by distribution matching, but applied post-processing (e.g., semi global block matching) to obtain continuous estimates.

Stereo-based 3D object detection. 3D object detection has attracted significant attention recently, especially for the application of self-driving cars [3, 5, 9, 10, 15, 39]. While many algorithms rely on the expensive LiDAR sensor as input [17, 18, 32, 37, 50], several recent papers have shown promising accuracy using the much cheaper stereo images [8, 16, 19, 21, 31, 45, 48]. One particular framework is Pseudo-LiDAR [33, 42, 54], which converts stereo depth estimates into a 3D point cloud that can be inputted to any existing LiDAR-based detector, achieving the state-of-the-art results.

3 Disparity Estimation

For brevity, in the following we mainly discuss disparity estimation. The same technique can easily be applied to depth estimation, which is usually adapted from their disparity estimation counterparts.

As reviewed in [section 2](#), many existing stereo networks output a distribution of disparities at each pixel. This distribution is a categorical distribution over discrete disparity values: discrete because they are estimated as the difference in X -coordinates of corresponding pixels, and as such are integers. Stereo techniques then compute the mean of the distribution to obtain a continuous estimate that is not limited to integral values.

We point out two disadvantages of taking the mean estimate. First, the mean value can deviate from the mode and may wrongly predict values of low probability when the predicted distribution is multi-modal (see [Figure 3](#)). Such multi-modal distributions appear frequently at pixels around the object boundaries.

While they collectively occupy only a tiny portion of image pixels, recent studies have shown their particular importance in the downstream tasks like 3D object detection [20, 21, 33]. For instance, let us consider a street scene where a car 30m away (a disparity of, say, 10 pixels) is driving on the road towards the camera, with the sky as the background. The pixels on the car boundary can either take a disparity of around 10 pixels (for the car) or a disparity of 0 pixels (for the sky). Simply taking the mean likely produces arbitrary disparity estimates between these values, producing depth estimates that are neither on the car nor on the background. The downstream 3D object detector can, therefore, wrongly predict the car orientation and size, potentially leading to accidents. Second, the physical meaning of the mean value is by no means aligned with the true disparity: uncertainty in correspondence might yield a 40% chance of a disparity of 10 pixels and a 60% chance for a disparity of 20 pixels, but this does not mean that the disparity should be 16 pixels.

Instead, a more straightforward way to simultaneously model the uncertainty and output continuous disparity estimates is to extend the support of the output distribution beyond integers.

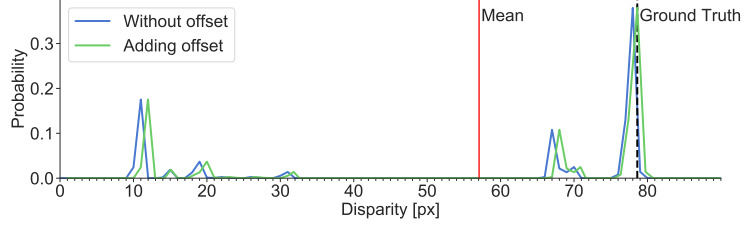


Figure 3: **The predicted disparity posterior for a pixel on object boundaries.** The uni-modal assumption can break down, leading to a *mean* estimate that is in a low probability region. Learning offsets allow us to predict the continuous *mode*. (Offsets are in $[0, 1]$ here.)

3.1 Continuous disparity network (CDN)

To this end, we propose a new neural network architecture and output representation for disparity estimation. The output of our network will still be a set of discrete values with corresponding probabilities, but the discrete values *will not be restricted to integers*. The key idea is to start with integral disparity values, and predict *offsets* in addition to probabilities.

Denote by \mathcal{D} the set of integral disparity values. As above, disparity estimation techniques produce a cost $S_{\text{disp}}(u, v, d)$ for every $d \in \mathcal{D}$. A softmax converts this cost into a probability distribution:

$$p(d|u, v) = \begin{cases} \text{softmax}(-S_{\text{disp}}(u, v, d)) & \text{if } d \in \mathcal{D}, \\ 0 & \text{otherwise.} \end{cases} \quad (5)$$

We propose to add a sub-network $b(u, v, d)$ that predicts an offset disparity value for each integral disparity value $d \in \mathcal{D}$ at each pixel (u, v) . We use this to displace the probability mass at $d \in \mathcal{D}$ to $d' = d + b(u, v, d)$. This results in the following probability distribution:

$$\tilde{p}(d'|u, v) = \sum_{d \in \mathcal{D}} p(d|u, v) \delta(d' - (d + b(u, v, d))), \quad (6)$$

which is a mixture of Dirac delta functions over arbitrary disparity values d' . In other words, \tilde{p} has $|\mathcal{D}|$ supports, each located at $d + b(u, v, d)$ with a weight $p(d|u, v)$. The resulting continuous disparity estimate $D(u, v)$ at (u, v) is the **mode** of $\tilde{p}(d'|u, v)$.

Our network design with a sub-network for offset prediction is reminiscent of G-RMI pose estimator [30] and one-stage 2D object detectors [22, 24, 35]. The former predicts the heatmaps (at fixed locations) and offsets for each keypoint; the latter parameterizes the predicted bounding box coordinates by the anchor box location plus the predicted offset. One may also interpret our approach as a coarse-to-fine depth prediction, first picking the bin centered around $\arg\max_{d \in \mathcal{D}} p(d|u, v)$ and then locally adjusting it by an offset.

In our implementation, the sub-network $b(u, v, d)$ shares its feature and computation with $S_{\text{disp}}(u, v, d)$ except for the last block of fully-connected or convolutional layers.

3.2 Learning with Wasserstein distances

We propose to train our disparity network such that the mixture of Dirac delta functions (Equation 6) is directly learned to match the ground truth distribution. Concretely, we represent the distribution of ground truth disparity at a pixel (u, v) , $p^*(d'|u, v)$, as a Dirac delta function centered at the ground truth disparity $d^* = D^*(u, v)$: $p^*(d'|u, v) = \delta(d' - d^*)$. We then employ a learning objective to minimize the divergence (distance) between $\tilde{p}(d'|u, v)$ and $p^*(d'|u, v)$. There are many popular divergence measures between distributions, such as Kullback-Leibler divergence, Jensen-Shannon divergence, total Variation, the Wasserstein distance, etc. In this paper, we choose the Wasserstein distance for one particular reason: $\tilde{p}(d'|u, v)$ and $p^*(d'|u, v)$ may not have any common supports.

The Wasserstein- p distance between two distributions μ, ν over a metric space (X, d) is defined as

$$W_p(\mu, \nu) = \left(\inf_{\gamma \in \Gamma(\mu, \nu)} \mathbb{E}_{\gamma} d(x, y)^p \right)^{1/p}, \quad (7)$$

where $\Gamma(\mu, \nu)$ denotes the set of all the joint distributions $\gamma(x, y)$ whose marginal distributions $\gamma(x)$ and $\gamma(y)$ are exactly μ and ν , respectively. Intuitively, $\gamma(x, y)$ indicates how much “mass” to be transported from x to y in order to transform the distribution μ to ν .

Estimating the Wasserstein distance is usually non-trivial and requires solving a linear programming problem. One particular exception is when μ and ν are both distributions of one-dimensional variables, which is the case for our distribution over disparity values². Specifically, when ν is a Dirac delta function whose support is located at y^* , the Wasserstein- p distance can be simplified as

$$W_p(\mu, \nu) = (\mathbb{E}_{\mu} \mathbb{E}_{\nu} \|x - y\|^p)^{1/p} = (\mathbb{E}_{\mu} \|x - y^*\|^p)^{1/p}. \quad (8)$$

By plugging $\tilde{p}(d'|u, v)$ and $p^*(d'|u, v)$ into μ and ν respectively, we obtain

$$\begin{aligned} W_p(\tilde{p}, p^*) &= (\mathbb{E}_{\tilde{p}} \|d' - d^*\|^p)^{1/p} = \left(\sum_{d \in \mathcal{D}} p(d|u, v) \|d + b(u, v, d) - d^*\|^p \right)^{1/p} \\ &= \left(\sum_{d \in \mathcal{D}} \text{softmax}(-S_{\text{disp}}(u, v, d)) \|d + b(u, v, d) - d^*\|^p \right)^{1/p}, \end{aligned} \quad (9)$$

based on which we can learn the conventional disparity network (red) and the additional offset sub-network (blue) jointly (i.e., by minimizing Equation 9). We focus on W_1 and W_2^2 distances.

3.3 Extension: learning with multi-modal ground truths

One particular advantage of learning to match the distributions is the capability of allowing multiple ground truth values (i.e., a multi-modal ground truth distribution) at a single pixel location. Denote \mathcal{D}^* as the set of ground truth disparity values at a pixel (u, v) , the ground truth distribution becomes

$$p^*(d'|u, v) = \sum_{d^* \in \mathcal{D}^*} \frac{1}{|\mathcal{D}^*|} \delta(d' - d^*). \quad (10)$$

Since $p^*(d'|u, v)$ is not a Dirac delta function, we can no longer apply Equation 8 but the following equation for comparing two one-dimensional distributions [29, 34, 44]

$$W_p(\tilde{p}, p^*) = \left(\int_0^1 \left| \tilde{P}^{-1}(x) - P^{*-1}(x) \right|^p dx \right)^{1/p}, \quad (11)$$

where \tilde{P} and P^* are the cumulative distribution functions (CDFs) of \tilde{p} and p^* , respectively. For the case $p = 1$, we can rewrite Equation 11 as [40]

$$W_1(\tilde{p}, p^*) = \int_{\mathbb{R}} \left| \tilde{P}(d') - P^*(d') \right| dd'. \quad (12)$$

²For dealing with disparity or depth values at a pixel, our metric space naturally becomes \mathcal{R}^1 .

We note that, both Equation 11 and Equation 12 can be computed efficiently.

While existing datasets do not provide multi-modal ground truths directly, we investigate the following procedure to construct them. For each pixel, we consider a $k \times k$ neighborhood and create a multi-modal distribution by setting the center-pixel disparity with a weight α and the remaining ones each with $\frac{1-\alpha}{k \times k - 1}$. We set $k = 3$ and $\alpha = 0.8$ in the experiment. Our empirical study shows that using a multi-modal ground truth leads to a much faster model convergence.

3.4 Comparisons to related work

Kendall et al. [14] discussed the use of means or modes. They employed pre-scaling to sharpen the predicted probability, which might resolve the multi-modal issue but makes the prediction concentrate on discrete disparity values. In contrast, we do not prevent predicting a multi-modal distribution, especially for pixels whose disparities are inherently multi-modal. We output the mode (after an offset), which is what Kendall et al. [14] hoped to achieve. We note that 3D convolutions can smooth the estimation but cannot guarantee uni-modal distributions.

Compared to G-RMI pose estimator and one-stage 2D object detectors mentioned in subsection 3.1, our work learns the two (sub-)networks jointly using a single objective function rather than a combination of two separated ones. See the supplementary material for more comparisons. Liu et al. [25] propose to use the Wasserstein loss for pose estimation to characterize the inter-class correlations; however, they do not predict offsets for pre-defined discrete pose labels. Our work is also related to [2], in which the authors propose to learn the value distribution, instead of the expected value, using the Wasserstein loss for reinforcement learning.

4 Experiments

4.1 Datasets and metrics

Datasets. We evaluate our method on two challenging stereo benchmark datasets, i.e., Scene Flow [27] and KITTI 2015 [28], and on a 3D object detection benchmark KITTI 3D [9, 10].

1) Scene Flow [27]. Scene Flow is a large synthetic dataset containing 35,454 training image pairs and 4,370 testing image pairs, where the ground truth disparity maps are densely provided, which is large enough for directly training deep neural networks.

2) KITTI 2015 [28]. KITTI 2015 is a real-world dataset with street scenes captured from a driving car. KITTI 2015 contains 200 training stereo image pairs with sparse ground truth disparities obtained using LiDAR, and 200 testing image pairs with ground truth disparities held by evaluation server for submission evaluation only. Its small size makes it a challenging dataset.

3) KITTI 3D [9, 10]. KITTI 3D contains 7,481 (pairs of) images for training and 7,518 (pairs of) images for testing. We follow the same training and validation splits as suggested by Chen et al. [6], containing 3,712 and 3,769 images, respectively. For each image, KITTI provides the corresponding Velodyne LiDAR point cloud (for sparse depth ground truths), camera calibration matrices, and 3D bounding box annotations. We evaluate our approach by plugging it into existing stereo-based 3D object detectors [8, 42, 54], which all require stereo depth estimation as a key component.

Metrics. We evaluate our methods on three tasks: stereo disparity estimation, stereo depth estimation, and 3D object detection. We apply the corresponding standard metrics listed as follows.

1) stereo disparity. we use two standard metrics: End-Point-Error (EPE), i.e., the average difference of the predicted disparities and their true ones, and k -Pixel Threshold Error (PE), i.e., the percentage of pixels for which the predicted disparity is off the ground truth by more than k pixels. We use the 1-pixel and 3-pixel threshold errors, denoted as 1PE and 3PE. PE is robust to outliers with large disparity errors, while EPE measures errors to sub-pixel level.

2) stereo depth. We use the Root Mean Square Error (RMSE) $\sqrt{\frac{1}{|\mathcal{A}|} \sum_{(u,v) \in \mathcal{A}} |z(u,v) - z^*(u,v)|^2}$ and Absolute Relative Error (ABSR) $\frac{1}{|\mathcal{A}|} \sum_{(u,v) \in \mathcal{A}} \frac{|z(u,v) - z^*(u,v)|}{z^*(u,v)}$, where \mathcal{A} denotes all the pixels having ground truths, and z and z^* are estimated depth and ground truth depth respectively.

3) 3D object detection. We focus on 3D and bird’s-eye-view (BEV) localization and report the results on the official leader board and the validation set. Specifically, we focus on the “car” category,

Table 1: **Disparity results.** We report results on Scene Flow and KITTI 2015. For Scene Flow, end point errors (EPE) and the 1-pixel and 3-pixel threshold error rates (1PE, 3PE) are reported. For KITTI 2015 we report the standard metrics (using 3PE) for both Non-occluded and All pixels regions. Methods based on **CDN** are highlighted in blue. Lower is better. The best result per column in in bold. *Since the baselines are mostly trained with uni-modal ground truths, we only show CDN with the same ground truths here for a fair comparison.*

Method	Scene Flow			KITTI 2015			
	EPE	1PE	3PE	Non Occlusion 3PE		All Areas 3PE	
				Foreground	All	Foreground	All
MC-CNN [56]	3.79	-	-	7.64	3.33	8.88	3.89
GC-Net [14]	2.51	16.9	9.34	5.58	2.61	6.16	2.87
PSMNet [4]	1.09	12.1	4.56	4.31	2.14	4.62	2.32
SegStereo [52]	1.45	-	-	3.70	2.08	4.07	2.25
GwcNet-g [11]	0.77	8.0	3.30	3.49	1.92	3.93	2.11
HD ³ -Stereo [53]	1.08	-	-	3.43	1.87	3.63	2.02
GANet [57]	0.84	9.9	-	3.37	1.73	3.82	1.93
AcfNet [58]	0.87	-	4.31	3.49	1.72	3.80	1.89
Stereo Expansion [51]	-	-	-	3.11	1.63	3.46	1.81
GANet Deep [57]	0.78	8.7	-	3.11	1.63	3.46	1.81
CDN-PSMNet	0.98	9.1	3.99	4.01	2.12	4.34	2.29
CDN-GANet Deep	0.70	7.7	2.98	2.79	1.72	3.20	1.92

following [7, 47]. We report the average precision (AP) at IoU thresholds 0.5 and 0.7. We denote AP for the 3D and BEV tasks by AP_{3D} and AP_{BEV} , respectively. The benchmark defines for each category three cases — easy, moderate, and hard — according to the bounding box height and occlusion and truncation. In general, the easy cases correspond to cars within 30 meters of the ego-car distance.

4.2 Implementation details

We mainly use the Wasserstein-1 distance (i.e., W_1 loss) for training our **CDN** model. We compare W_1 and W_2^2 losses in the supplementary material.

Stereo disparity. We apply our **continuous disparity network (CDN)** architecture to PSMNet [4] and GANet [57], namely **CDN-PSMNET** and **CDN-GANET**. To keep a fair comparison, we train the models with their default settings. For Scene Flow, the models are trained from scratch with a constant learning rate of 0.001 for 10 epochs. For KITTI 2015, the models pre-trained on Scene Flow are fine-tuned following the default strategy of the vanilla models. We consider disparities in the range of $[0, 191]$ for both datasets. We use a uniform grid of bin size 2 pixels to create the categorical distribution (cf. Equation 5). We show the effect of bin sizes in the supplementary material.

Stereo depth. We apply **CDN** to the SDN architecture [54], namely **CDN-SDN**. We follow the training procedure in [54]. We consider depths in the range of $[0m, 80m]$. We use a uniform grid of bin size 1m to create the categorical distribution.

The offset sub-network. We implement $b(u, v, d)$ with a Conv3D-Relu-Conv3D block. It takes the 4D cost volume, before the last fully-connected or convolutional block of $S_{disp}(u, v, d)$, as the input. We predict a single offset $b(u, v, d) \in [0, s]$ for each integral disparity value d , where s is the bin size. We achieve this by clipping. The sub-network has 30K parameters, only 0.3% w.r.t. PSMNET [4]. For stereo depth, we implement $b(u, v, z) \in [0, s]$ in the same way for each integral depth value z .

Stereo 3D object detection. We apply **CDN-SDN** to PSEUDO-LIDAR ++ [54], which uses SDN to estimate depth. We fine-tune the **CDN-SDN** model pre-trained on Scene Flow on KITTI 3D dataset, followed by using a 3D object detector, here P-RCNN [37], to detect 3D bounding boxes of cars. We also apply **CDN** to DSGN [8], the state-of-the-art stereo-based 3D object detector. DSGN uses as a backbone depth estimator based on PSMNET and we replace it with our **CDN** version.

Multi-modal ground truths. As mentioned in subsection 3.3, we create multi-modal ground truths for a pixel by considering a patch in its $k \times k$ neighborhood. We give the center-pixel disparity a weight $\alpha = 0.8$, and the remaining ones an equal weight such that the total sums to 1. In this case, we use Equation 12 as the loss function. We implement a differentiable loss module in Pytorch that can be applied to a batch of image tensors. Please see the supplementary material for more details.

Table 2: **3D object detection results on the KITTI leader board.** We report AP_{BEV} and AP_{3D} (in %) of the car category at $IoU = 0.7$. Methods with **CDN** are in blue. The best result of each column is in bold font.

Method	BEV Detection AP (AP_{BEV})			3D Detection AP (AP_{3D})		
	Easy	Moderate	Hard	Easy	Moderate	Hard
S-RCNN [21]	61.9	41.3	33.4	47.6	30.2	23.7
OC-STEREO [31]	68.9	51.5	43.0	55.2	37.6	30.3
DISP R-CNN [38]	74.1	52.4	43.8	59.6	39.4	32.0
PSEUDO-LiDAR [42]	67.3	45.0	38.4	54.5	34.1	28.3
PSEUDO-LiDAR ++ [54]	78.3	58.0	51.3	61.1	42.4	37.0
PSEUDO-LiDAR E2E [33]	79.6	58.8	52.1	64.8	43.9	38.1
CDN-PSEUDO-LiDAR ++	81.3	61.0	52.8	64.3	44.9	38.1
DSGN [8]	82.9	65.0	56.6	73.5	52.2	45.1
CDN-DSGN	83.3	66.2	57.7	74.5	54.2	46.4

Table 3: **Disparity multi-modal results.** We report the EPE, 1PE and 3PE on Scene Flow. Methods with **CDN** are highlighted in blue. The best result of each column is in bold font.

Method	EPE	1PE	3PE	Method	EPE	1PE	3PE
PSMNET [4]	1.09	12.1	4.56	GANET Deep [57]	0.78	8.7	-
CDN-PSMNET	0.98	9.1	3.99	CDN-GANET Deep	0.70	7.7	2.98
CDN-PSMNET MM	0.96	9.0	3.96	CDN-GANET Deep MM	0.68	7.7	2.97

4.3 Main results

Disparity estimation. Table 1 summarizes the results on disparity estimation. **CDN-GANET Deep**³ achieves the lowest error at all three metrics on Scene Flow. It reduces the error for GANET Deep by 1.0 1PE and 0.08 EPE, both are significant. We see a similar gain for PSMNET: **CDN-PSMNET** reduces EPE by 0.09, demonstrating the general applicability of our approach to existing networks.

On KITTI 2015, **CDN-GANET Deep** obtains the lowest error on the *foreground* pixels and performs comparably to other methods on all the pixels⁴. We see a similar gain by **CDN-PSMNET** over PSMNET on the foreground, which is quite surprising, as we do not specifically *re-weight* the loss function towards foreground pixels. Since **CDN** has advantages on pixels whose disparity is ambiguous and hard to estimate correctly (e.g., due to multi-modal distributions), the fact that foreground pixels have a higher error and **CDN** can effectively reduce it suggests that those challenging pixels are mostly in the foreground. As will be seen in 3D object detection, the improvement by **CDN** on foreground pixels translates to a higher accuracy on localizing objects.

3D object detection. Table 2 summarizes the results on the test set of KITTI 3D. Our **CDN** consistently improves the two mainstream approaches, namely, DSGN and PSEUDO-LiDAR. For PSEUDO-LiDAR, we achieve a 2.5%/3.0% gain on AP_{3D}/AP_{BEV} Moderate (the standard metric on the leader board) against PSEUDO-LiDAR ++: the only difference is that we replace SDN by our **CDN-SDN** to have better depth estimates. Our approach even outperforms PSEUDO-LiDAR E2E, which fine-tunes the depth network specifically for object detection. We argue that our approach, which can *automatically* focus on the foregrounds, may have a similar effect as end-to-end training with object detection losses. For DSGN, plugging our **CDN-SDN** leads to a notable 2% gain at AP_{3D} , attaining the highest entry of stereo-based 3D detection accuracy on the KITTI leader board.

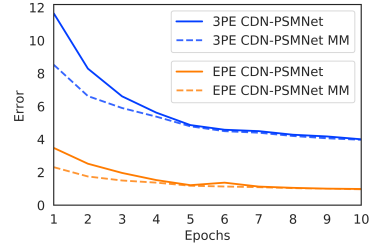


Figure 4: **MM training.** We show the EPE and 3PE disparity errors on Scene Flow test set using **CDN-PSMNET**, w/ or w/o MM training. MM training leads to faster convergence.

³We apply the GANET Deep model introduced in the released code of [57], available at <https://github.com/feihuzhang/GANet>. The main architectures of GANET Deep and GANET are the same, while the former has some more 2D and 3D convolutional layers.

⁴There are two possible reasons that **CDN-GANET Deep** does not outperform GANET Deep on all the pixels. First, **CDN** overly focuses on foreground pixels. Second, we used the same hyper-parameters as the original GANET without specific tuning for **CDN**. We note that the ratio of foreground/background pixels is $\sim 0.15/0.85$; the degradation by **CDN** on the background is ~ 0.16 3PE, smaller than the gain on foreground.

Table 4: **Depth multi-modal results.** We report the RMSE and ABSR errors on Scene Flow. The best result of each column is in bold font.

Method	RMSE (m)	ABSR
SDN [54]	2.05	0.039
CDN-SDN	1.81	0.030
CDN-SDN MM	1.80	0.028

4.4 Analysis

Multi-modal (MM) ground truth. We investigate creating the multi-modal (MM) ground truths for training our models. Table 3 and Table 4 summarize the results on Scene Flow for disparity and depth estimation, respectively. MM training slightly reduces the errors. To better understand how MM ground truths affect network training, we plot the test accuracy along the training epochs in Figure 4: CDN-PSMNET trained with MM ground truths converges much faster. We attribute this to the observations in [1]: a neural network tends to learn simple and *clean* patterns first. We note that, for boundary pixels whose disparities are inherently multi-modal, uni-modal ground truths are indeed *noisy* labels. A network thus tends to ignore these pixels in the early epochs. In contrast, MM ground truths provide *clean* supervisions for these boundary pixels; the network thus can learn the patterns much faster. See the supplementary material for a visualization and further discussions.

Ablation studies. We study different components of our approach in Table 6. Methods without W_1 loss use the regression loss for optimization (cf. Equation 2) and output the mean. Methods with W_1 loss output the mode. We see that, the offset sub-network alone can hardly improve the performance. Using W_1 distance alone reduces 1PE and 3PE errors, but not EPE, suggesting that it cannot produce sub-pixel disparity estimates⁵. Only combining the offset sub-network and the W_1 loss produces consistent improvement over all three metrics.

Disparity on boundaries. Table 5 shows the results: we obtain pixels on object boundaries using the OpenCV Canny edge detector with minVal/maxVal=100/200. Both CDN and training with multi-modal ground truths reduce the error significantly.

Qualitative disparity results on KITTI. As shown in Figure 5, our approach is able to estimate disparity accurately, especially along the object boundaries. Specifically, CDN-GANET Deep maintains the straight bar shape (on the right), while GANET Deep blends it with the background sky due to the mean estimates.

5 Conclusion

In this paper we have introduced a new output representation, model architecture and loss function for depth/disparity estimation that can faithfully produce real-valued estimates of depth/disparity. We have shown that results not just in more accurate depth estimates, but also significant improvement in downstream tasks like object detection. Finally, because we explicitly output and optimize a distribution over depths, our approach can naturally take into account *uncertainty and multimodality* in the ground truth. More generally, our results suggest that removing suboptimalities in how we represent and optimize 3D information can have a large impact on a multitude of vision tasks.

Table 5: **Ambiguous regions (object boundaries).** We report the disparity error on Scene Flow. The best result of each column is in bold font.

Method	EPE	1PE	3PE
PSMNet [4]	3.10	20.1	11.33
CDN-PSMNet	2.10	15.3	8.92
CDN-PSMNet MM	2.08	13.2	8.65

Table 6: **Ablation studies.** We report disparity error for CDN-PSMNET on Scene Flow. Methods without W_1 loss are learned with *mean* regression.

Offsets	W_1 Loss	Output	EPE	1PE	3PE
✓		Mean	1.09	12.1	4.56
		Mean	1.04	12.0	4.55
✓	✓	Mode	1.20	10.5	4.21
		Mode	0.98	9.1	3.99

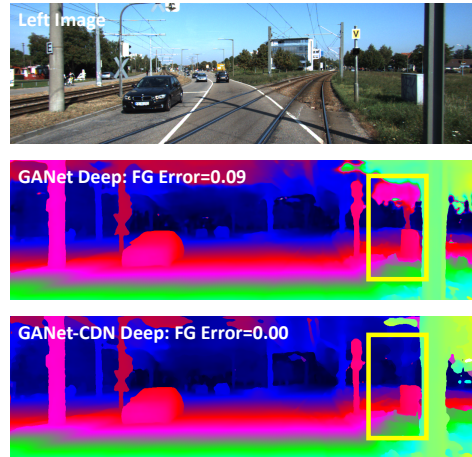


Figure 5: **Qualitative results on disparity.** The top, middle, and bottom images are the left image, the result of GANET Deep, and the result of CDN-GANET Deep, together with the foreground 3PE.

⁵Using a bin size $s = 2$ without offsets, the mode is restricted to integral values and EPE suffers.

Broader Impact

The end results of this paper are improved depth and disparity estimation, particularly on foreground objects. This is of use to self-driving cars, 3D reconstruction, and other robotics applications. In particular, it has the potential to improve the *safety* of these systems, as indicated by the increased 3D object detection performance. Our approach can also easily be incorporated into other depth or disparity estimation algorithms for further improvement.

While our depth predictions are significantly better, any failure has important safety considerations, such as collisions and accidents. Before deployment, appropriate safety thresholds must be cleared.

Our approach does not specifically leverage dataset biases, although being a machine learning approach, it is impacted as much as other machine learning techniques.

Acknowledgments

This research is supported by grants from the National Science Foundation NSF (III-1618134, III-1526012, IIS-1149882, IIS-1724282, and TRIPODS-1740822, OAC-1934714), the Office of Naval Research DOD (N00014-17-1-2175), the Bill and Melinda Gates Foundation, and the Cornell Center for Materials Research with funding from the NSF MRSEC program (DMR-1719875). We are thankful for generous support by Zillow, SAP America Inc, AWS Cloud Credits for Research, Ohio Supercomputer Center, and Facebook.

References

- [1] Devansh Arpit, Stanisław Jastrzebski, Nicolas Ballas, David Krueger, Emmanuel Bengio, Maxinder S Kanwal, Tegan Maharaj, Asja Fischer, Aaron Courville, Yoshua Bengio, et al. A closer look at memorization in deep networks. In *ICML*, 2017. 9
- [2] Marc G Bellemare, Will Dabney, and Rémi Munos. A distributional perspective on reinforcement learning. In *ICML*, 2017. 6
- [3] Holger Caesar, Varun Bankiti, Alex H. Lang, Sourabh Vora, Venice Erin Liong, Qiang Xu, Anush Krishnan, Yu Pan, Giancarlo Baldan, and Oscar Beijbom. nuscenes: A multimodal dataset for autonomous driving. *arXiv preprint arXiv:1903.11027*, 2019. 3
- [4] Jia-Ren Chang and Yong-Sheng Chen. Pyramid stereo matching network. In *CVPR*, 2018. 1, 2, 3, 7, 8, 9
- [5] Ming-Fang Chang, John W Lambert, Patsorn Sangkloy, Jagjeet Singh, Slawomir Bak, Andrew Hartnett, De Wang, Peter Carr, Simon Lucey, Deva Ramanan, and James Hays. Argoverse: 3d tracking and forecasting with rich maps. In *CVPR*, 2019. 3
- [6] Xiaozhi Chen, Kaustav Kundu, Yukun Zhu, Andrew G Berneshawi, Huimin Ma, Sanja Fidler, and Raquel Urtasun. 3d object proposals for accurate object class detection. In *NIPS*, 2015. 6
- [7] Xiaozhi Chen, Huimin Ma, Ji Wan, Bo Li, and Tian Xia. Multi-view 3d object detection network for autonomous driving. In *CVPR*, 2017. 7
- [8] Yilun Chen, Shu Liu, Xiaoyong Shen, and Jiaya Jia. Dsgn: Deep stereo geometry network for 3d object detection. In *CVPR*, 2020. 1, 3, 6, 7, 8
- [9] Andreas Geiger, Philip Lenz, and Raquel Urtasun. Are we ready for autonomous driving? the kitti vision benchmark suite. In *CVPR*, 2012. 2, 3, 6
- [10] Andreas Geiger, Philip Lenz, Christoph Stiller, and Raquel Urtasun. Vision meets robotics: The kitti dataset. *The International Journal of Robotics Research*, 32(11):1231–1237, 2013. 3, 6
- [11] Xiaoyang Guo, Kai Yang, Wukui Yang, Xiaogang Wang, and Hongsheng Li. Group-wise correlation stereo network. In *CVPR*, 2019. 7

- [12] Omid Hosseini Jafari, Oliver Groth, Alexander Kirillov, Michael Ying Yang, and Carsten Rother. Analyzing modular cnn architectures for joint depth prediction and semantic segmentation. In *ICRA*, 2017. 15
- [13] Jianbo Jiao, Ying Cao, Yibing Song, and Rynson Lau. Look deeper into depth: Monocular depth estimation with semantic booster and attention-driven loss. In *ECCV*, 2018. 15
- [14] Alex Kendall, Hayk Martirosyan, Saumitro Dasgupta, Peter Henry, Ryan Kennedy, Abraham Bachrach, and Adam Bry. End-to-end learning of geometry and context for deep stereo regression. In *ICCV*, 2017. 1, 2, 3, 6, 7
- [15] R. Kesten, M. Usman, J. Houston, T. Pandya, K. Nadhamuni, A. Ferreira, M. Yuan, B. Low, A. Jain, P. Ondruska, S. Omari, S. Shah, A. Kulkarni, A. Kazakova, C. Tao, L. Platinsky, W. Jiang, and V. Shet. Lyft level 5 av dataset 2019. [urlhttps://level5.lyft.com/dataset/](https://level5.lyft.com/dataset/), 2019. 3
- [16] Hendrik Königshof, Niels Ole Salscheider, and Christoph Stiller. Realtime 3d object detection for automated driving using stereo vision and semantic information. In *2019 IEEE Intelligent Transportation Systems Conference (ITSC)*, 2019. 3
- [17] Jason Ku, Melissa Mozifian, Jungwook Lee, Ali Harakeh, and Steven Waslander. Joint 3d proposal generation and object detection from view aggregation. In *IROS*, 2018. 3
- [18] Alex H Lang, Sourabh Vora, Holger Caesar, Lubing Zhou, Jiong Yang, and Oscar Beijbom. Pointpillars: Fast encoders for object detection from point clouds. In *CVPR*, 2019. 3
- [19] Buyu Li, Wanli Ouyang, Lu Sheng, Xingyu Zeng, and Xiaogang Wang. Gs3d: An efficient 3d object detection framework for autonomous driving. In *CVPR*, 2019. 3
- [20] Peiliang Li, Tong Qin, et al. Stereo vision-based semantic 3d object and ego-motion tracking for autonomous driving. In *ECCV*, 2018. 4
- [21] Peiliang Li, Xiaozhi Chen, and Shaojie Shen. Stereo r-cnn based 3d object detection for autonomous driving. In *CVPR*, 2019. 1, 3, 4, 8
- [22] Tsung-Yi Lin, Priya Goyal, Ross Girshick, Kaiming He, and Piotr Dollár. Focal loss for dense object detection. In *ICCV*, 2017. 2, 4, 15
- [23] Miaomiao Liu, Xuming He, and Mathieu Salzmann. Geometry-aware deep network for single-image novel view synthesis. In *CVPR*, 2018. 1
- [24] Wei Liu, Dragomir Anguelov, Dumitru Erhan, Christian Szegedy, Scott Reed, Cheng-Yang Fu, and Alexander C Berg. Ssd: Single shot multibox detector. In *ECCV*, 2016. 2, 4, 15
- [25] Xiaofeng Liu, Yang Zou, Tong Che, Peng Ding, Ping Jia, Jane You, and BVK Kumar. Conservative wasserstein training for pose estimation. In *ICCV*, 2019. 6
- [26] Wenjie Luo, Alexander G Schwing, and Raquel Urtasun. Efficient deep learning for stereo matching. In *CVPR*, 2016. 3
- [27] Nikolaus Mayer, Eddy Ilg, Philip Hausser, Philipp Fischer, Daniel Cremers, Alexey Dosovitskiy, and Thomas Brox. A large dataset to train convolutional networks for disparity, optical flow, and scene flow estimation. In *CVPR*, 2016. 1, 2, 6
- [28] Moritz Menze and Andreas Geiger. Object scene flow for autonomous vehicles. In *CVPR*, 2015. 6
- [29] Victor M Panaretos and Yoav Zemel. An invitation to statistics in wasserstein space, 2020. 5
- [30] George Papandreou, Tyler Zhu, Nori Kanazawa, Alexander Toshev, Jonathan Tompson, Chris Bregler, and Kevin Murphy. Towards accurate multi-person pose estimation in the wild. In *CVPR*, 2017. 1, 2, 4, 15
- [31] Alex D Pon, Jason Ku, Chengyao Li, and Steven L Waslander. Object-centric stereo matching for 3d object detection. In *ICRA*, 2020. 3, 8

- [32] Charles R Qi, Wei Liu, Chenxia Wu, Hao Su, and Leonidas J Guibas. Frustum pointnets for 3d object detection from rgb-d data. In *CVPR*, 2018. 3
- [33] Rui Qian, Divyansh Garg, Yan Wang, Yurong You, Serge Belongie, Bharath Hariharan, Mark Campbell, Kilian Q Weinberger, and Wei-Lun Chao. End-to-end pseudo-lidar for image-based 3d object detection. In *CVPR*, 2020. 1, 3, 4, 8
- [34] Aaditya Ramdas, Nicolás García Trillos, and Marco Cuturi. On wasserstein two-sample testing and related families of nonparametric tests. *Entropy*, 19(2):47, 2017. 5
- [35] Joseph Redmon, Santosh Divvala, Ross Girshick, and Ali Farhadi. You only look once: Unified, real-time object detection. In *CVPR*, 2016. 2, 4, 15
- [36] Daniel Scharstein and Richard Szeliski. High-accuracy stereo depth maps using structured light. In *CVPR*, 2003. 1
- [37] Shaoshuai Shi, Xiaogang Wang, and Hongsheng Li. Pointcnn: 3d object proposal generation and detection from point cloud. In *CVPR*, 2019. 3, 7
- [38] Jiaming Sun, Linghao Chen, Yiming Xie, Siyu Zhang, Qinhong Jiang, Xiaowei Zhou, and Hujun Bao. Disp r-cnn: Stereo 3d object detection via shape prior guided instance disparity estimation. In *CVPR*, 2020. 8
- [39] Pei Sun, Henrik Kretschmar, Xerxes Dotiwalla, Aurelien Chouard, Vijaysai Patnaik, Paul Tsui, James Guo, Yin Zhou, Yuning Chai, Benjamin Caine, et al. Scalability in perception for autonomous driving: Waymo open dataset. In *CVPR*, 2020. 3
- [40] Matthew Thorpe. Introduction to optimal transport. 2018. 5
- [41] Cédric Villani. *Optimal transport: old and new*, volume 338. Springer Science & Business Media, 2008. 2
- [42] Yan Wang, Wei-Lun Chao, Divyansh Garg, Bharath Hariharan, Mark Campbell, and Kilian Q. Weinberger. Pseudo-lidar from visual depth estimation: Bridging the gap in 3d object detection for autonomous driving. In *CVPR*, 2019. 1, 3, 6, 8
- [43] Yan Wang, Zihang Lai, Gao Huang, Brian H Wang, Laurens van der Maaten, Mark Campbell, and Kilian Q Weinberger. Anytime stereo image depth estimation on mobile devices. In *ICRA*, 2019. 1, 3
- [44] Larry Wasserman. Lecture notes in statistical methods for machine learning, 2019. 5
- [45] Bin Xu and Zhenzhong Chen. Multi-level fusion based 3d object detection from monocular images. In *CVPR*, 2018. 3
- [46] Dan Xu, Wanli Ouyang, Xiaogang Wang, and Nicu Sebe. Pad-net: Multi-tasks guided prediction-and-distillation network for simultaneous depth estimation and scene parsing. In *CVPR*, 2018. 15
- [47] Danfei Xu, Dragomir Anguelov, and Ashesh Jain. Pointfusion: Deep sensor fusion for 3d bounding box estimation. In *CVPR*, 2018. 7
- [48] Zhenbo Xu, Wei Zhang, Xiaoqing Ye, Xiao Tan, Wei Yang, Shilei Wen, Errui Ding, Ajin Meng, and Liusheng Huang. Zoomnet: Part-aware adaptive zooming neural network for 3d object detection. In *AAAI*, 2020. 3
- [49] Koichiro Yamaguchi, David McAllester, and Raquel Urtasun. Efficient joint segmentation, occlusion labeling, stereo and flow estimation. In *ECCV*, 2014. 2
- [50] Bin Yang, Wenjie Luo, and Raquel Urtasun. Pixor: Real-time 3d object detection from point clouds. In *CVPR*, 2018. 3
- [51] Gengshan Yang and Deva Ramanan. Upgrading optical flow to 3d scene flow through optical expansion. In *ICCV*, 2020. 7

- [52] Guorun Yang, Hengshuang Zhao, Jianping Shi, Zhidong Deng, and Jiaya Jia. SegStereo: Exploiting semantic information for disparity estimation. In *ECCV*, 2018. 7
- [53] Zhichao Yin, Trevor Darrell, and Fisher Yu. Hierarchical discrete distribution decomposition for match density estimation. In *CVPR*, 2019. 7
- [54] Yurong You, Yan Wang, Wei-Lun Chao, Divyansh Garg, Geoff Pleiss, Bharath Hariharan, Mark Campbell, and Kilian Q Weinberger. Pseudo-lidar++: Accurate depth for 3d object detection in autonomous driving. In *ICLR*, 2020. 1, 2, 3, 6, 7, 8, 9, 16
- [55] Ye Yu and William AP Smith. Depth estimation meets inverse rendering for single image novel view synthesis. In *European Conference on Visual Media Production*, 2019. 1
- [56] Jure Zbontar and Yann LeCun. Stereo matching by training a convolutional neural network to compare image patches. *JMLR*, 17:1–32, 2016. 2, 7
- [57] Feihu Zhang, Victor Prisacariu, Ruigang Yang, and Philip HS Torr. Ga-net: Guided aggregation net for end-to-end stereo matching. In *CVPR*, 2019. 1, 2, 3, 7, 8
- [58] Youmin Zhang, Yimin Chen, Xiao Bai, Jun Zhou, Kun Yu, Zhiwei Li, and Kuiyuan Yang. Adaptive unimodal cost volume filtering for deep stereo matching. In *AAAI*, 2020. 3, 7
- [59] Xingyi Zhou, Dequan Wang, and Philipp Krähenbühl. Objects as points. *arXiv preprint arXiv:1904.07850*, 2019. 15

Supplementary Material

We provide in this material the contents omitted in the main paper:

- **Appendix A:** additional implementation details (cf. subsection 3.2 and subsection 4.2 of the main paper).
- **Appendix B:** additional discussions (cf. section 3 and subsection 4.4 of the main paper).
- **Appendix C:** additional experimental results and analysis (cf. subsection 4.2, subsection 4.3, and subsection 4.4 of the main paper).

A Implementation Details

A.1 Learning with multi-modal ground truths

For multi-modal ground truths, we cannot use Equation 8 of the main paper for optimization. Instead, we apply the loss in Equation 12, for W_1 distance. This loss essentially computes the difference in areas between the CDFs of the two distributions. For mixtures of Dirac delta functions, it can be efficiently implemented by computing the accumulated difference between CDF histograms. It takes $\mathcal{O}(B \log B)$ for each pixel using sorting, where B is the total number of supports of both distributions. Our implementation is adapted from `scipy.stats.wasserstein_distance` and we modify it to be compatible with Pytorch tensors and use CUDA to parallelize the computation over all the pixels.

A.2 Learning with the (approximated) KL divergence

The *Kullback–Leibler* (KL) divergence

$$KL(\mu||\nu) = \mathbb{E}_\mu \log(\mu||\nu) \quad (13)$$

between two distributions μ and ν requires them to have the same supports: i.e., $\mu(d') = 0$ if $\nu(d') = 0$, for $KL(\mu||\nu)$ to be finite.

For our case, $\mu(d') = \delta(d' - d^*)$ and $\nu(d') = \sum_{d \in \mathcal{D}} p(d|u, v) \delta(d' - (d + b(u, v, d)))$. These two measures may have different supports. To make the KL divergence applicable, we can smooth ν to form a mixture of Laplace or Gaussian distributions.

For example, smoothing ν with a Laplace distribution, $\text{Laplace}(0, \tau) = \frac{1}{2\tau} \exp\left(-\frac{|d'|}{\tau}\right)$, we get

$$\nu_{\text{Lap}}(d') = \sum_{d \in \mathcal{D}} p(d|u, v) \frac{1}{2\tau} \exp\left(-\frac{|d' - (d + b(u, v, d))|}{\tau}\right). \quad (14)$$

With ν_{Lap} , the KL divergence reduces to the following loss

$$\ell(\mu, \nu_{\text{Lap}}) = -\log \sum_{d \in \mathcal{D}} p(d|u, v) \frac{1}{2\tau} \exp\left(-\frac{|d^* - (d + b(u, v, d))|}{\tau}\right) \quad (15)$$

$$\approx -\log p(\bar{d}|u, v) + \frac{1}{\tau} |d^* - (\bar{d} + b(u, v, \bar{d}))|, \quad (16)$$

where $\bar{d} = s \lfloor \frac{d^*}{s} \rfloor \in \mathcal{D}$ is the grid disparity value of the bin the true disparity d^* belongs to.

Similarly, smoothing ν with a Gaussian distribution $\mathcal{N}(0, \sigma^2)$, we get

$$\nu_{\text{Gau}}(d') = \sum_{d \in \mathcal{D}} p(d|u, v) \frac{1}{\sigma\sqrt{2\pi}} \exp\left(-\frac{\|d' - (d + b(u, v, d))\|_2^2}{2\sigma^2}\right). \quad (17)$$

With ν_{Gau} , the KL divergence reduces to the following loss

$$\ell(\mu, \nu_{\text{Gau}}) = -\log \sum_{d \in \mathcal{D}} p(d|u, v) \frac{1}{\sigma\sqrt{2\pi}} \exp\left(-\frac{\|d^* - (d + b(u, v, d))\|_2^2}{2\sigma^2}\right) \quad (18)$$

$$\approx -\log p(\bar{d}|u, v) + \frac{1}{2\sigma^2} \|d^* - (\bar{d} + b(u, v, \bar{d}))\|_2^2, \quad (19)$$

where $\bar{d} = s \lfloor \frac{d^*}{s} \rfloor \in \mathcal{D}$ is the grid disparity value of the bin the true disparity d^* belongs to.

These formulations reduce to the conventional classification loss plus offset regression loss, commonly used for keypoint estimation [30, 59] and one-stage 2D object detection [22, 24, 35, 59].

B Additional Discussions

B.1 Multi-modal ground truths

There are three reasons why multi-modal ground truths would benefit disparity or depth estimation. First, pixels are discrete: a single pixel may capture different depths. Second, real datasets need to project signals from a depth sensor (e.g., LiDAR) to a depth map. As pixels are discrete and the cameras and LiDAR might be placed differently, multiple LiDAR points of different depths may be projected to the same pixel. Third, for stereo estimation, pixels along boundaries or occluded regions cause ambiguity to the model; multi-modal ground truths offer better supervision for training, especially in early training epochs.

Conceptually, learning with multi-modal ground truths should notably improve results in Table 3 and Table 4 of the main paper. However, in evaluation, a majority of pixels are not on the object boundaries. Besides, we still evaluate using the (likely noisy) uni-modal ground truths. To further analyze these, we show in Table 6 of the main paper the disparity error calculated on object boundaries: learning with multi-modal ground truths leads to a significant improvement.

B.2 Multi-task learning

One way to mitigate stereo predictions at depth discontinuities is to jointly perform stereo estimation and other tasks such as semantic segmentation [12, 13, 46], which can reason about object boundaries. The core idea is to leverage additional semantic labels to guide the model to resolve depth discontinuities (i.e., predict uni-modal distributions). Our method, in contrast, does not prevent predicting multi-modal distributions along depth discontinuities, but changes the outputting rule (i.e., argmin with a predicted offset). Our method can also capture depth discontinuities within an object or an object class. In contrast, semantic segmentation labels overlapped objects of the same class by the same label and does not directly tell their boundaries.

B.3 Offsets and distributions without common supports

While the *learned* offsets may lead to common supports between the predicted and ground truth distributions, we have to first come up with a loss to *learn* such offsets before common supports become possible. Concretely, to learn $b(u, v, d)$ in Equation 9, we need a loss that can measure the divergence between \bar{p} and p^* , which may not have common supports. We note that, this may occur even if the target distribution p^* is a Dirac delta function. While the KL divergence or a regression loss may be applied to learn the offsets, they need to either smooth the distributions or carefully design the loss to learn both the distribution and the offset networks. The Wasserstein distance offers a principled loss to learn the two networks jointly.

C Additional Results and Analysis

C.1 Ablation studies on different divergences

We show the ablation study on using different divergences between distributions in Table 7. For the KL divergence (subsection A.2), we use Laplace smoothing with $b = 1$ (Equation 16). Our results show that the Wasserstein distance is a better choice than the KL divergence for comparing the predicted and the ground truth disparity (or depth) distributions. We also see that W_2^2 distance performs worse than W_1 . We attribute this to outliers (i.e., noisy disparity labels) in a dataset.

C.2 Effect of bin sizes

CDN outputs modes and needs (a) the bin containing the truth disparity or depth to have the highest probability and (b) the offset to be accurate. The bin size balances the difficulty of (a) and (b). A

Table 7: **Comparison of different divergences (distances).** We report the RMSE and the ABSR error for depth estimation on Scene Flow. The best result of each column is in bold font.

Method	Divergence	RMSE (m)	ABSR
SDN	-	2.05	0.04
CDN-SDN	KL	2.57	0.04
CDN-SDN	W_1	1.81	0.03
CDN-SDN	W_2^2	1.91	0.05

Table 8: **Comparison of bin sizes.** We report the disparity error on Scene Flow using **CDN-PSMNET** model.

Bin size	EPE	1PE	3PE
1	1.22	13.9	4.33
2	0.98	9.1	3.99
4	1.52	26.1	4.17

smaller bin size makes (a) harder. A larger bin size makes (a) easier but makes (b) harder as the range of offsets gets larger. It is the only hyper-parameter to tune and only integral values are considered.

We show these effects of bin sizes on uniform grids, with disparities in the range of $[0, 191]$ for disparity estimation in Table 8. For a bin size $s = 1$, predicting the correct bin is harder. For a bin size $s = 4$, predicting the correct bin is easier, whereas predicting the correct offset becomes harder. We found $s = 2$ to perform well in general.

C.3 Ablation studies on α and k in multi-modal (MM) ground truths

Table 9 shows the depth estimation error on Scene Flow using **CDN-SDN-MM**, with different α and k in preparing the MM ground truths (cf. Table 4 of the main paper). A smaller α leads to a larger error, which makes sense as it relies less on the ground truths.

C.4 Learning with multi-modal (MM) ground truths

Following subsection 4.4 and Figure 4 of the main paper, we train **CDN-PSMNET** and **CDN-PSMNET MM** for only two epochs and compare their disparity estimation performance. Figure 6 shows the results on KITTI images. While both methods have similar predictions at smooth regions, **CDN-PSMNET MM** leads to much sharper and clearer object boundaries, suggesting that the multi-modal ground truths are better supervisions for learning around the boundaries in early epochs.

C.5 Learned offsets

The offset network learns to produce the sub-grid disparity at each integral disparity values. Figure 7 shows an example, in which we back-project pixels into 3D points using the estimated disparity or depth at each pixel by the *mode*, with or without the offset prediction. Without the offset, the 3D points can only occupy discrete depths, leading to a discontinuous, non-smooth point cloud.

C.6 Point cloud visualization

Figure 8 shows the BEV point cloud visualization. We show the 3D points generated by SDN and **CDN-SDN** as well as the ground truth LiDAR points and car/pedestrian boxes. We see that, **CDN-SDN** generates sharper points than SDN. Specifically for pixels on the foreground objects, SDN usually predicts the depths beyond the boxes due to the *mean* estimates from multi-modal distributions on the boundary pixels, whereas **CDN-SDN** significantly alleviates the problem. We also see some failure cases of **CDN-SDN**: on the right image, **CDN-SDN** has a larger error on the background compared to SDN.

C.7 Depth estimation

Besides the Scene Flow dataset, we show the depth estimation error on KITTI Val: the 3,769 validation images for 3D object detection. We follow [54] to train the depth estimation model and compute the depth estimation error on pixels associated with ground truth LiDAR points. Table 10



Figure 6: **Qualitative results on learning with multi-modal ground truths at early epochs.** The top, middle, and bottom images are the left image, the result of **CDN-PSMNET**, and the result of **CDN-PSMNET MM**.

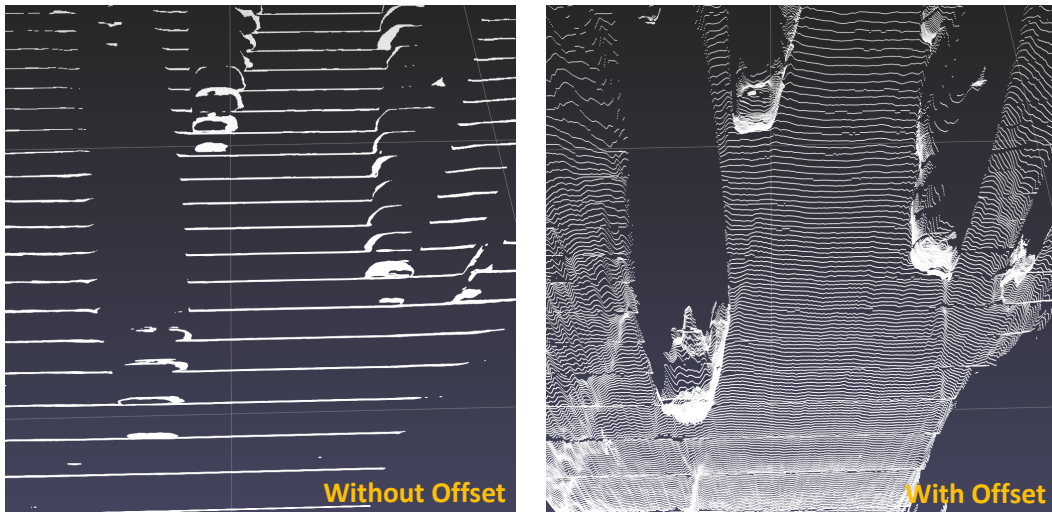


Figure 7: A visualization of the 3D point cloud (from the bird's-eye view) derived from the estimated disparities or depths (by modes), with (right) and without (left) offset prediction.

Table 9: **Ablation studies on the MM ground truths.** We conduct experiments using **CDN-SDN** MM on Scene Flow (cf. Table 4 of the main paper).

α	k	RMSE	ABSR
0.8	3	1.80	0.028
0.8	5	1.82	0.029
0.8	7	1.88	0.035
0.5	3	1.81	0.029
0.2	3	2.20	0.062

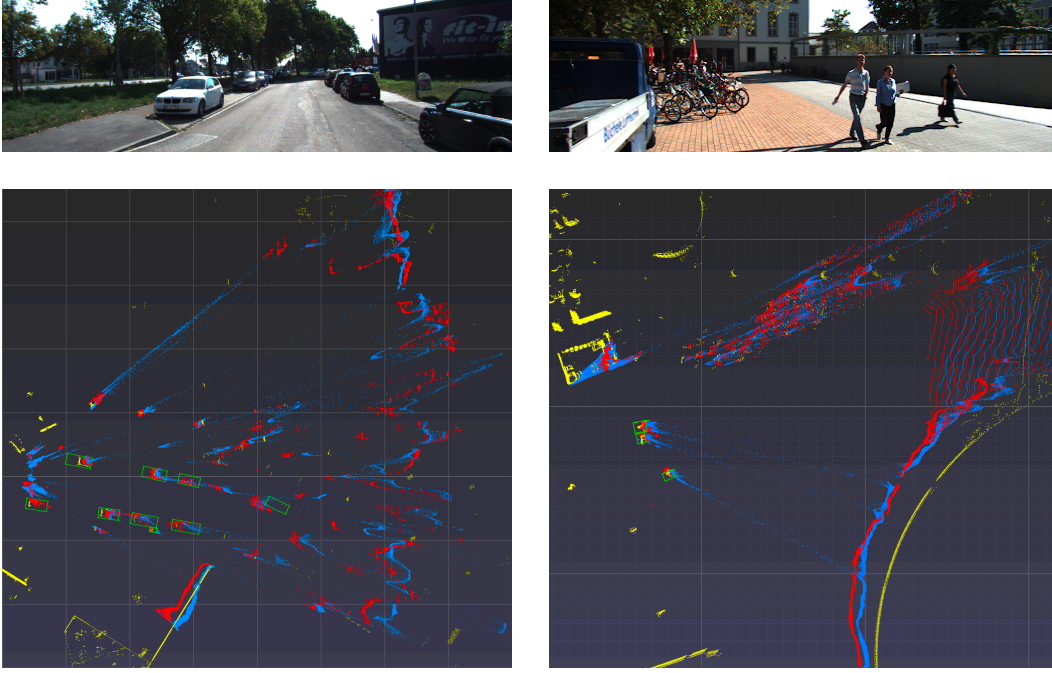


Figure 8: **BEV Point cloud visualization.** The blue points are obtained using SDN. The red points are from our **CDN-SDN** model. The yellow points are from the ground truth LiDAR. The green boxes are ground truth car / pedestrian locations. The observer is at the left-hand side of the point cloud looking to the right.

and **Figure 9** show the results, **CDN-SDN** achieves lower error than SDN, which explains why **CDN-SDN** (and **CDN-DSGN**) can lead to better 3D object detection accuracy.

C.8 3D object detection

We show in **Figure 10** the object detection precision-recall curves of DSGN vs. **CDN-DSGN**. **CDN-DSGN** has higher precision (vertical) values than DSGN at different recall (horizontal) values.

C.9 Qualitative disparity results

We show in **Figure 11** and **Figure 12** the predicted disparity maps and the foreground errors of both GANET Deep and **CDN-GANET** Deep on KITTI and Scene Flow. **CDN** generally leads to sharper and clearer object boundaries.

Table 10: **Depth error on KITTI Val.** We compare SDN and **CDN-SDN** models.

Method	Depth errors (m)			
	Mean	Median	RMSE	ABSR
SDN	0.589	0.128	3.08	0.044
CDN-SDN	0.524	0.093	3.00	0.042

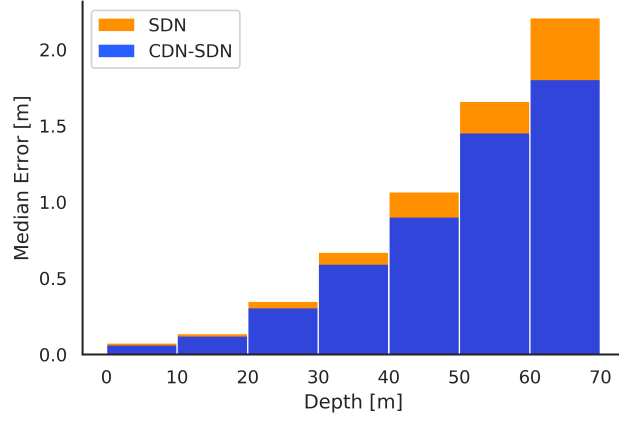


Figure 9: **Depth error on KITTI Val.** We compute the median absolute depth error for different depth ranges on KITTI Val images using SDN and **CDN-SDN**.

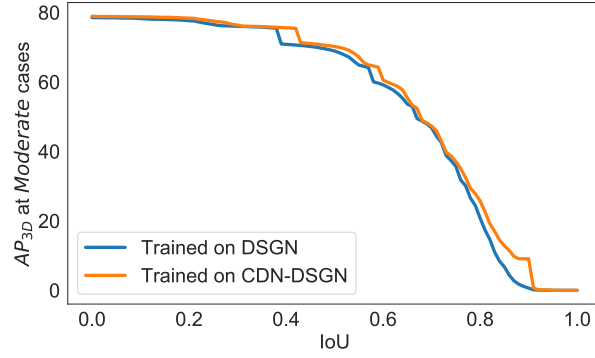


Figure 10: We show the object detection precision-recall curves for AP_{3D} at moderate cases on cars. We compare DSGN (stereo images) and **CDN-DSGN** (stereo images).

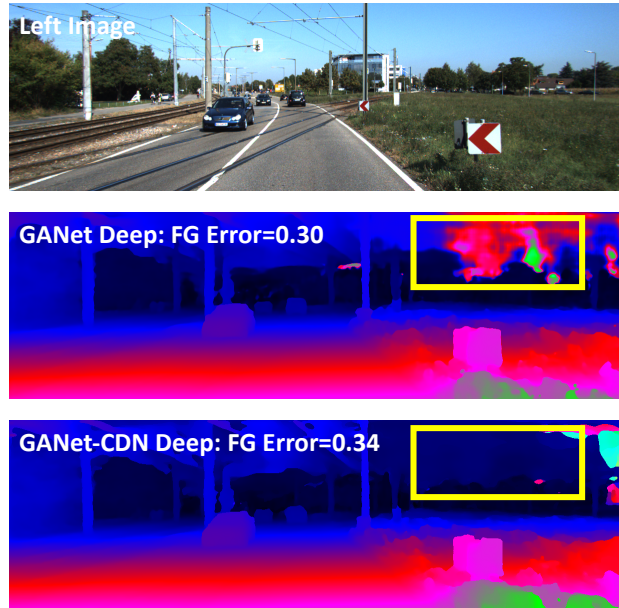


Figure 11: **Qualitative results on KITTI.** The top, middle, and bottom images are the left image, the result of GANET Deep, and the result of **CDN-GANET Deep**, together with the foreground 3PE.

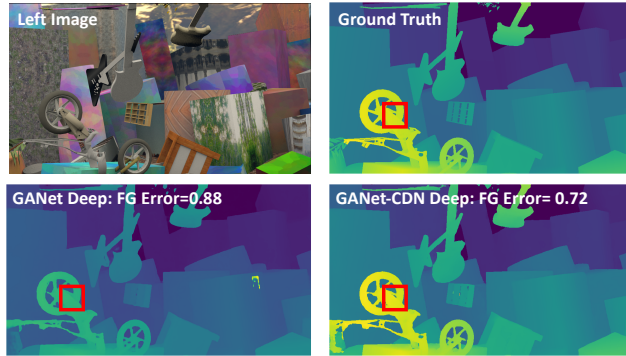


Figure 12: **Qualitative results on Scene Flow validation set.** The first row shows the left image and the ground truth map. The second row shows the result of GANet Deep and the result of **CDN-GANet** Deep, together with the foreground end point errors (EPE).